SAND2019-7777C
Proceedings of the ASME 2019
International Technical Conference on Packaging and Integration of Electronic and Photonic Microsystems
InterPACK2019
October 7-9, 2019, Anaheim, CA, USA

InterPACK2019-6440

INTEGRATED OPTICAL PROBING OF THE THERMAL DYNAMICS OF WIDE BANDGAP POWER ELECTRONICS

James Spencer Lundh[1], Yiwen Song[1], Bikram Chatterjee[1], Albert G. Baca[2], Robert J. Kaplar[2], Andrew A. Allerman[2], Andrew M. Armstrong [2], Hyungtak Kim[3], and Sukwon Choi[1]

[1]Department of Mechanical Engineering, The Pennsylvania State University, University Park, Pennsylvania, 16802, USA
[2]Sandia National Laboratories, Albuquerque, New Mexico, 87185, USA
[3]School of Electronic and Electrical Engineering, Hongik University, 94, Wausan-ro, Mapo-gu, Seoul, 04066, Korea

ABSTRACT

Researchers have been extensively studying wide-bandgap (WBG) semiconductor materials such as gallium nitride (GaN) with an aim to accomplish an improvement in size, weight, and power (SWaP) of power electronics beyond current devices based on silicon (Si). However, the increased operating power densities and reduced areal footprints of WBG device technologies result in significant levels of self-heating that can ultimately restrict device operation through performance degradation, reliability issues, and failure. Typically, self-heating in WBG devices is studied using a single measurement technique while operating the device under steady-state direct current (DC) measurement conditions. However, for switching applications, this steady-state thermal characterization may lose significance since high power dissipation occurs during fast transient switching events. Therefore, it can be useful to probe the WBG devices under transient measurement conditions in order to better understand the thermal dynamics of these systems in practical applications. In this work, the transient thermal dynamics of an AlGaN/GaN high electron mobility transistor (HEMT) were studied using thermoreflectance thermal imaging and Raman thermometry. Also, the proper use of iterative pulsed measurement schemes such as thermoreflectance thermal imaging to determine the steady-state operating temperature of devices is discussed. These studies are followed with subsequent transient thermal characterization to accurately probe the self-heating from steady-state down to sub-microsecond pulse conditions using both thermoreflectance thermal imaging and Raman thermometry with temporal resolutions down to 15 ns.

Keywords: Gallium nitride (GaN), high electron mobility transistor (HEMT), power electronics, Raman thermometry, self-heating, thermal dynamics, thermal management, thermoreflectance thermal imaging, wide bandgap (WBG)

NOMENCLATURE

E_g	Bandgap energy
2DEG	Two-dimensional electron gas
C_{TR}	Thermoreflectance coefficient
τ_{delay}	LED pulse temporal location
τ_{on}	Electrical pulse width
I_{aS}/I_S	Anti-Stokes/Stokes Raman intensity ratio
P	Power density
V_{DS}	Drain-source voltage
V_{GS}	Gate-source voltage

1. INTRODUCTION

Wide bandgap semiconductor materials such as silicon carbide (SiC) and gallium nitride (GaN) have been replacing silicon (Si) as the standard material in high frequency and high power electronics [1]–[7]. While SiC has high thermal conductivity [8] suggesting superior thermal performance, GaN has reasonably high thermal conductivity [8] in addition to numerous superior electronic properties. These include its wide bandgap (E_g ~3.4 eV), high breakdown field, and high saturation velocity [8]–[11]. These material properties are promising for high temperature, high voltage, and high frequency operation. Furthermore, due to spontaneous and piezoelectric polarization effects in AlGaN/GaN heterostructures [12], [13], high electron mobility transistor (HEMT) structures can be fabricated that utilize a two-dimensional electron gas (2DEG) as the device current channel. The high carrier concentration and mobility in the 2DEG results in reduced sheet resistance, lowering conduction losses [14]–[16]. The high breakdown field also allows fabrication of shorter channel devices; in combination with the high saturation velocity and high mobility, this can lead to reduced switching losses [14]–[16].

However, the concurrent benefits of size reduction and high voltage and high current operation are also accompanied by aggravated device self-heating. Extreme localized heat generation due to the electric field concentration near the drain-side corner of the gate structure results in intense heat fluxes and significant temperature rise [17]–[21].

Self-heating is detrimental to device performance and poses reliability issues. It degrades electrical performance due to the temperature dependence of the electrical properties such as electron mobility [22]. Self-heating also compromises the mechanical stability of the devices due to the induction of thermal stresses arising from the mismatch in the thermal expansion coefficients of GaN and the substrate material [23], [24]. Furthermore, the combination of thermal, piezoelectric, and residual stresses can also cause electrical performance degradation due to defect creation or a critical total stress can be reached at which point there is catastrophic failure [25], [26]. As such, self-heating is inherently a reliability issue which degrades performance and reduces component mean-time-to-failure [27].

Experimental analysis of both the steady-state and transient device thermal response are crucial to understand device electrothermomechanical interactions and electrical implications associated with self-heating. Moreover, accurate thermal characterization enables calibration with multi-physics models to determine peak operating temperatures which are used for lifetime assessment [27], [28] and to analyze the effectiveness of thermal management solutions [29]–[31]. In addition, these models can be used to better understand the coupled electrothermal device physics which can be difficult or impossible to study experimentally. Therefore, it is necessary to confidently and accurately characterize the thermal response of the devices to better understand the device physics and ensure long-term and stable operation.

Several thermal characterization techniques are commonly used to quantify self-heating in electronics including infrared thermography, Raman thermometry, and thermoreflectance thermal imaging [32]–[37]. While infrared thermography is the most common method employed, it has been shown to underestimate the peak temperature rise [37]–[39]. The temporal resolution of transient infrared thermography is limited to microsecond levels; therefore, it is not capable of capturing the thermal dynamics important in hard switching applications with rapid transient high power dissipation in the nanosecond regime [40], [41]. Raman thermometry is very effective as a point measurement technique to determine the temperature rise in the semiconductor channel under both steady-state [32], [33], [42] and transient [43], [44] measurement conditions. Thermoreflectance thermal imaging is also well-suited for steady-state and transient microelectronics temperature assessment due to the abundance of metallization structures and two-dimensional mapping capabilities [34], [45]. However, due to low signal-to-noise ratios, it commonly employs a iterative lock-in measurement scheme which forces synchronization of pulsed device operation and optical probing [46]. Improper use of this technique resulting from failure to fully understand the thermal dynamics of the system can result in reporting of quasi-steady state temperature rises in the device channel which can be significantly lower than the true steady-state value.

In this work, the thermal dynamics of an AlGaN/GaN HEMT will be studied through integrated transient optical probing using thermoreflectance thermal imaging and Raman thermometry. A brief review of the fundamental concepts of these techniques will be followed with a discussion concerning proper use of thermoreflectance thermal imaging for steady-state temperature quantification. This discussion will be succeeded by complete lateral and vertical transient thermal characterization using both thermoreflectance thermal imaging and Raman thermometry. The complete transient thermal analysis permits insight into the thermal dynamics present in the operating regimes of high power switching applications and potential thermal management approaches.

2. MATERIALS AND METHODS

Thermal characterization was performed on a single-finger AlGaN/GaN high electron mobility transistor (HEMT) using thermoreflectance thermal imaging and Raman thermometry. In order to optically probe the entire lateral and vertical domains of the device structure, variations of each technique were also used. Both visible and ultraviolet (UV) wavelength thermoreflectance thermal imaging were used to probe the metallization structures and GaN channel, respectively. Both standard Raman thermometry and nanoparticle-assisted Raman thermometry were used to probe the Si substrate and channel surface, respectively.

2.1 Device Description

The AlGaN/GaN HEMT was grown on a 650 μm thick Si substrate. A 4.3 μm thick GaN buffer was grown on the Si substrate followed by a 20 nm $Al_{0.23}Ga_{0.77}N$ barrier layer to form the 2DEG. The structure was capped with a 4 nm GaN layer and passivated with a 20 nm SiO_2 layer. Ti/Al/Ni/Au (20/100/25/50 nm) Ohmic contacts were formed with e-beam evaporation followed by rapid thermal annealing at 800 °C. A Ni/Au (20/200 nm) Schottky gate was also formed using e-beam evaporation with a gate length of 2 μm and a 1 μm gate-overhang on both the drain and source sides of the gate. The source-gate and drain-gate spacing are 3 μm and 15 μm, respectively. The gate width is 100 μm. Both a top-side view and a cross-sectional schematic of the device structure are shown in Fig. 1.

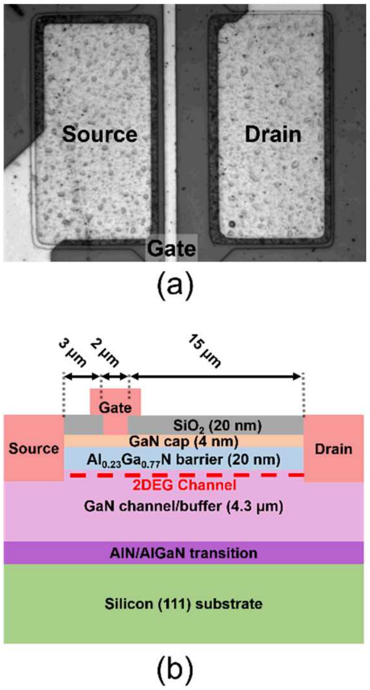

FIGURE 1: (a) Top-side and (b) cross-sectional view of the AlGaN/GaN high electron mobility transistor analyzed in the study.

2.2 Thermoreflectance Thermal Imaging

Thermoreflectance thermal imaging is ultimately governed by the temperature and wavelength dependence of the complex index of refraction. Experimentally, the temperature dependence of the reflectance of the material is measured using a CCD camera. This is because the complex index of refraction describes the reflectance of a material [47].

If the temperature dependence of the reflectance can be determined, the material temperature can be monitored. This relationship is established through the introduction of the thermoreflectance coefficient (C_{TR}) defined below [46], [47]:

$$C_{TR} = \frac{1}{R_0}\frac{\partial R}{\partial T} = \frac{1}{R_0}\frac{R-R_0}{T-T_0} \quad (1)$$

where R_0 and T_0 are the reflectance and temperature at the unpowered (cold) state and R and T are the reflectance and temperature at the powered (hot) state (Fig. 2). If the thermoreflectance coefficient is known and the reflectance at two different temperatures is measured, it follows that the temperature difference between these two states can be calculated. For example, the reflectance of the surface of a microelectronic device can be measured at a "hot" temperature during the ON-state and at a "cold" temperature during the OFF-state. Using the C_{TR} of the device surface and Eq. 1, the temperature rise of the device surface can be calculated. As mentioned above, the complex index of refraction and thus the reflectance is also wavelength dependent; this allows for the testing of various wavelengths to maximize the thermoreflectance coefficient.

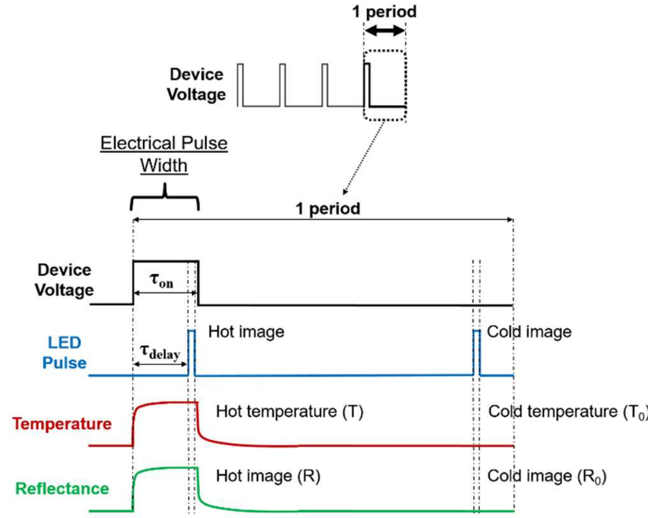

FIGURE 2: A schematic illustrating the synchronized electrical and LED pulsing in the lock-in modulation scheme employed for thermoreflectance thermal imaging. The top of the figure shows the repetitive cycling involved to accumulate the reflectance signal over many periods. The bottom of the figure highlights the pulse synchronization for one period.

However, the C_{TR} is still typically only on the order of 10^{-5} K^{-1} to 10^{-3} K^{-1}; therefore, it is desirable to enhance the signal-to-noise ratio by employing a lock-in modulation scheme [46]. In this measurement scheme (Fig. 2), an electrical pulse train biasing the device causes a repeated change in reflectance, and the "hot" and "cold" reflectance are repeatedly measured using a fixed LED pulse train that is synchronized with the electrical pulse train. The lock-in modulation allows the reflectance signal to be accumulated over many periods reducing the required measurement acquisition time. As such, thermoreflectance thermal imaging is an iterative measurement technique. This pulsed measurement technique can be easily transformed for transient thermal characterization by shifting the temporal location of the LED pulse (τ_{delay}) inside the device voltage electrical pulse width (τ_{on}) as shown in Fig. 2.

Thermoreflectance thermal imaging is uniquely applicable for the thermal characterization of microelectronics due to the abundance of highly reflective metallization structures. Also, by changing the LED illumination wavelength, more regions of the device can be probed. For example, the GaN channel region is transparent to visible wavelengths because the bandgap of GaN (~3.4 eV) is greater than the corresponding photonic energy of visible wavelengths. However, ultraviolet LED illumination wavelengths such as 365 nm (~3.4 eV) probe the GaN channel region and enable thermal measurements near the heat generation in the 2DEG channel located near the AlGaN/GaN heterointerface as shown in Fig. 1. Moreover, by using multiple illumination wavelengths, not only can the entire device surface be probed, but measurements results can also be validated by measuring a specific region with multiple LED illumination wavelengths.

In this study, thermoreflectance thermal imaging was conducted using a Microsanj NT-210A system equipped with a 3-axis piezo-controlled stage and a 1626 × 1236 pixel charge coupled-device (CCD) camera. Visible 530 nm LED illumination was used to probe the temperature of the metal gate, drain, and source contacts, and ultraviolet 365 nm LED illumination was used to probe the temperature of the GaN channel regions.

2.3 Raman Thermometry

Raman thermometry entails the use of Raman spectroscopy to perform temperature measurements. Raman spectroscopy uses monochromatic photonic excitation to probe the energy of the crystal lattice vibrations (phonons). Incident photons interact with the crystal lattice through scattering events. The vast majority of these scattering events are elastic: the photon incident upon the sample is emitted from the sample with no change in the photon energy (wavelength). This elastic scattering where the incident and emitted photons have the same energy is known as Rayleigh scattering. Much less frequently, these scattering events are inelastic: the photon incident upon the sample is emitted from the sample with either an increase or decrease in the photon energy. This inelastic scattering where the emitted photon has either gained or lost energy with respect to the incident photon is known as anti-Stokes or Stokes Raman scattering, respectively. The manifestation of these scattering processes in a typical Raman spectrum are shown in Fig. 3(a). As a consequence of the conversation of energy, the increase or decrease in the emitted photon energy with respect to the incident photon energy is due to the annihilation or creation of a phonon in the crystal. The difference in the incident and emitted photon energy is therefore indicative of the phonon energy (frequency) in the crystal [48].

There are a few effects of temperature on phonon characteristics that can be observed in Raman spectra. These include peak position shifts, peak broadening, and changes in the ratio of anti-Stokes/Stokes Raman peak intensities (I_{aS}/I_S) [32], [42]. These phonon characteristics and the effect of temperature are shown in Fig. 3(b). If the rate of change of these characteristics with temperature is known, changes in the Raman spectra between two states can be measured and used to determine a temperature change. For example, a semiconductor material in a microelectronic device could be measured with Raman spectroscopy during the unpowered OFF-state and during a biased ON-state and the change in the characteristics of the Raman spectra could be monitored to determine the operating temperature rise in the semiconductor. Among the three methods for measuring temperature with Raman spectroscopy, the peak position-based method is the most common. This is because the linewidth method has large measurement uncertainty and generally lower sensitivity to temperature, and the anti-Stokes/Stokes intensity ratio method requires expensive notch filters and longer acquisition times. The drawback of using the peak position-based method is that the Raman peak position is sensitive to both temperature and temperature-induced thermo-elastic stress which can lead to inaccuracies in the thermal measurement [32], [42]. However, this can be overcome using specialized forms of Raman thermometry such as nanoparticle-assisted Raman thermometry which will be discussed shortly.

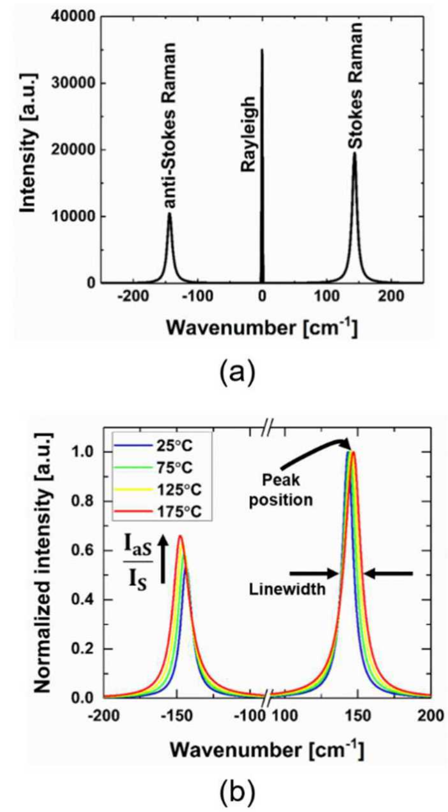

FIGURE 3: (a) A typical Raman spectrum showing (from left) anti-Stokes Raman, Rayleigh, and Stokes Raman peaks. (b) The effect of temperature on the peak position, linewidth, and anti-Stokes/Stokes intensity ratio (I_{aS}/I_S) in the Raman spectra. The spectra shown in (b) is the same as for (a) with the exception of the Rayleigh peak which has been removed. All Raman spectra shown are of a TiO_2 nanoparticle. The Raman peak observed at approximately ±145 cm^{-1} is the TiO_2 E_g phonon mode.

Similar to thermoreflectance thermal imaging, Raman thermometry is uniquely applicable for the thermal characterization of microelectronics because it can probe the temperature of the semiconductor materials of which these devices are based. If the laser wavelength and corresponding energy is less than the bandgap of the semiconductor, there is a finite amount of depth-averaging [49]. If the laser energy is above the bandgap of the semiconductor, the surface temperature will be measured as laser absorption will occur; in this case, laser heating and photocurrent induction must be considered. While Raman spectroscopy cannot be used to directly probe metals, nanoparticle-assisted Raman thermometry can be used to indirectly probe the temperatures of metals [50]. In addition, this variation of Raman thermometry can be used to measure the surface temperature of semiconductors whose bandgaps are greater than the laser energy of the Raman system. Nanoparticle-assisted Raman thermometry involves the deposition of nanoparticles on the surface of the device to be used as temperature transducers (Fig. 4). The nanoparticles are assumed to be in thermal equilibrium with the device surface, not alter the intrinsic temperature distribution, and experience negligible thermal stress. This facilitates the use of peak position-based methods for thermal characterization as there are no stress effects on the nanoparticle Raman peak positions.

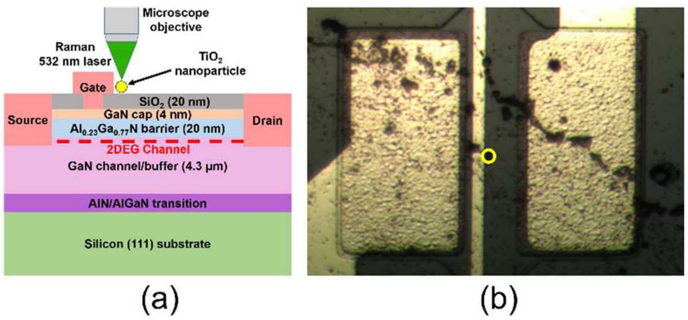

FIGURE 4: (a) Schematic of nanoparticle-assisted Raman thermometry showing the probing of the TiO_2 nanoparticle on the device surface using the Raman laser. (b) Optical image of TiO_2 nanoparticles deposited on the AlGaN/GaN HEMT. The yellow sphere and outline in (a) and (b), respectively, indicate the location of the TiO_2 nanoparticle measured in this study.

The standard Raman spectrometer can be used for steady-state thermal characterization, but with additional equipment Raman thermometry can be used for transient measurements (Fig. 5). The transient measurement experimental set-up in Fig. 5 adopts a lock-in modulation scheme similar to thermoreflectance thermal imaging in which the electrical and laser pulse trains are synchronized and the signal accumulates over many periods. Using the experimental set-up in Fig. 5, a temporal resolution of 15 ns was achieved and used in this study.

Both nanoparticle-assisted and standard Raman thermometry were used to probe the surface and Si substrate surface temperatures of the AlGaN/GaN HEMT, respectively. The surface temperature was probed using titanium dioxide (TiO_2) nanoparticles (99.98% purity) [50]. Raman thermometry was performed using a Horiba LabRAM HR Evolution spectrometer in a 180° backscattering configuration. The system is equipped with 532 nm laser excitation (2.33 eV) and measurements were performed with a long working distance 50X objective (NA = 0.45). To minimize the laser heating effect in the Si substrate and TiO_2 nanoparticles, a low laser power (~1 mW) was adopted. Systematic error was monitored and corrected using a reference mercury emission line at 546 nm.

3. RESULTS AND DISCUSSION

Since thermoreflectance thermal imaging is a pulsed measurement technique, it is important that the user ensures that the device under test is allowed to reach a true steady state condition. The device electrical pulse width (τ_{on}) set as a measurement input parameter for a fixed duty cycle (Fig. 2) should never be arbitrarily chosen; this should be determined by performing transient thermal characterization to analyze the transient thermal response of the device using various device electrical pulse widths. The electrical pulse width should be continually increased until there are no more increases in the

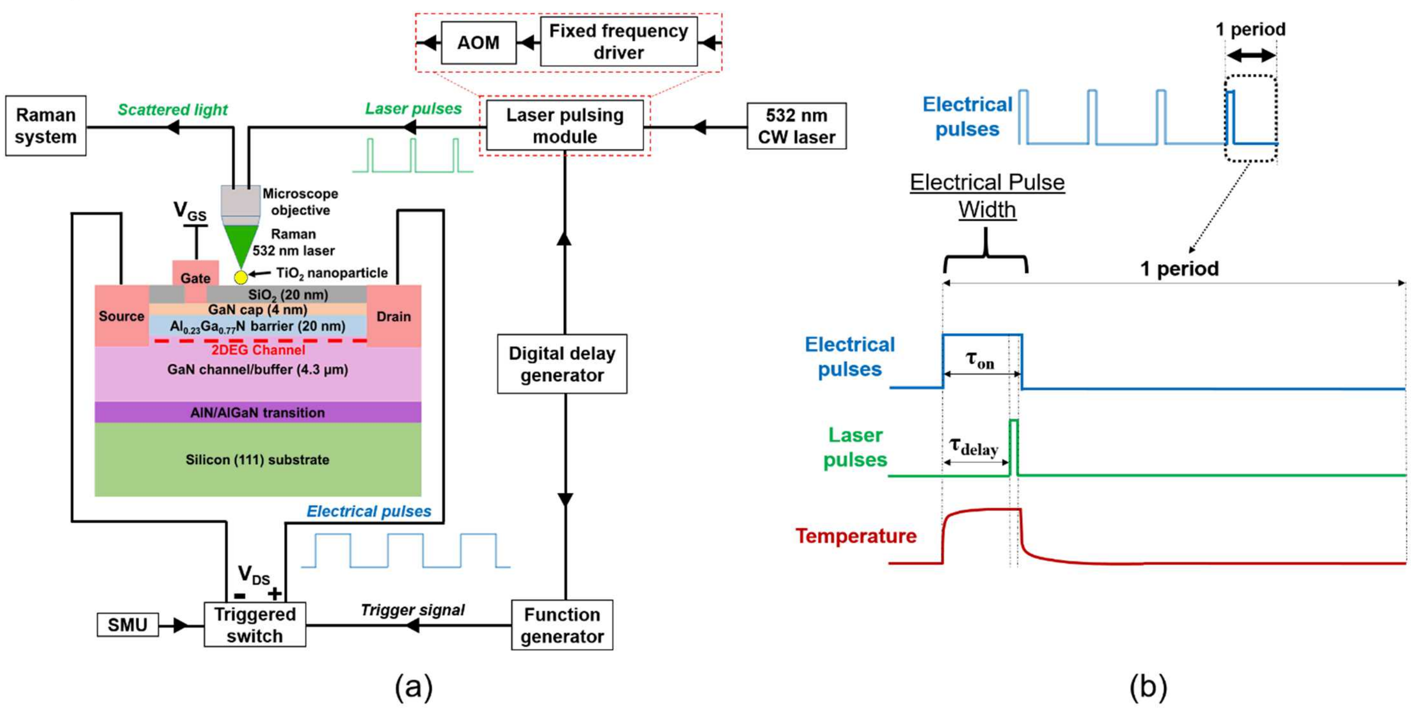

FIGURE 5: The (a) experimental set-up and (b) synchronized pulsing scheme used to enable transient measurements using Raman thermometry.

temperature measured at the end of the electrical pulse (T in Fig. 2). Also, the duty cycle selected should be low enough to ensure that the entire material stack has sufficient time to cool to the reference base temperature (T_0 in Fig. 2) before the reference reflectance signal (R_0 in Fig. 2) is measured. To determine the electrical pulse width, a small region of interest (ROI) is often selected on an important feature of the device to determine the pulse width at which no further increases in temperature are observed with increasing electrical pulse width; for the AlGaN/GaN HEMT used in this study, this feature would generally be the gate contact due to the localization of heat generation at the drain-side corner of the gate [17], [19], [51]. However, another important consideration is lateral heat spreading; while the gate may approach its steady state value at a given pulse width, other features of the device may not have reached the steady state temperature due to the thermal lag arising from the electrical pulse width dependent thermal penetration length, i.e., the lateral extent where temperature rise above the base plate temperature of the device under test (DUT) occurs as a result of lateral heat spreading This will be demonstrated using the AlGaN/GaN HEMT shown in Fig. 1 for electrical pulse widths of 10 μs, 100 μs, and 1000 μs. The AlGaN/GaN HEMT was biased to operate with a power density of P = 6 W/mm for all electrical pulse widths. The drain-source voltage (V_{DS}) was held constant at 28 V while the gate voltage (V_{GS}) was adjusted to maintain constant power density.

The transient thermal response of the AlGaN/GaN HEMT for each electrical pulse width is shown in Fig. 6 for ROIs on the gate and drain contacts. The temperature rise for each ROI shown is normalized with respect to the steady-state temperature rise for the respective ROI (i.e. $T_{Gate,\ 10\ \mu s}/T_{Gate,\ steady\text{-}state}$). For the electrical pulse width of 10 μs, it can be seen that neither the gate nor the drain contacts reach their steady state value. Furthermore, while the gate contact reaches almost 90% of its steady-state value in 10 μs, the drain contact only reaches approximately 50% of its steady state value due to the thermal lag imposed by the finite thermal penetration length. For the electrical pulse width of 100 μs, the thermal penetration length has increased and the thermal lag between the gate and drain contacts has reduced significantly as the gate and drain ROIs have respectively reached approximately 95% and 90% of their steady state temperature rise. It should be noted that if only the gate ROI was used, it would appear that the device has reached a steady state condition when in fact this is only a quasi-steady state condition in the vicinity of the heat source. As can be clearly seen from the drain ROI, the true device steady-state condition has not been reached. When the electrical pulse width is increased to 1000 μs, it is finally possible to observe that all features on the device surface have reached the true steady state condition. Careful consideration should be given to ensure that all regions of the device have reached a true steady state condition as shown in Fig. 6.

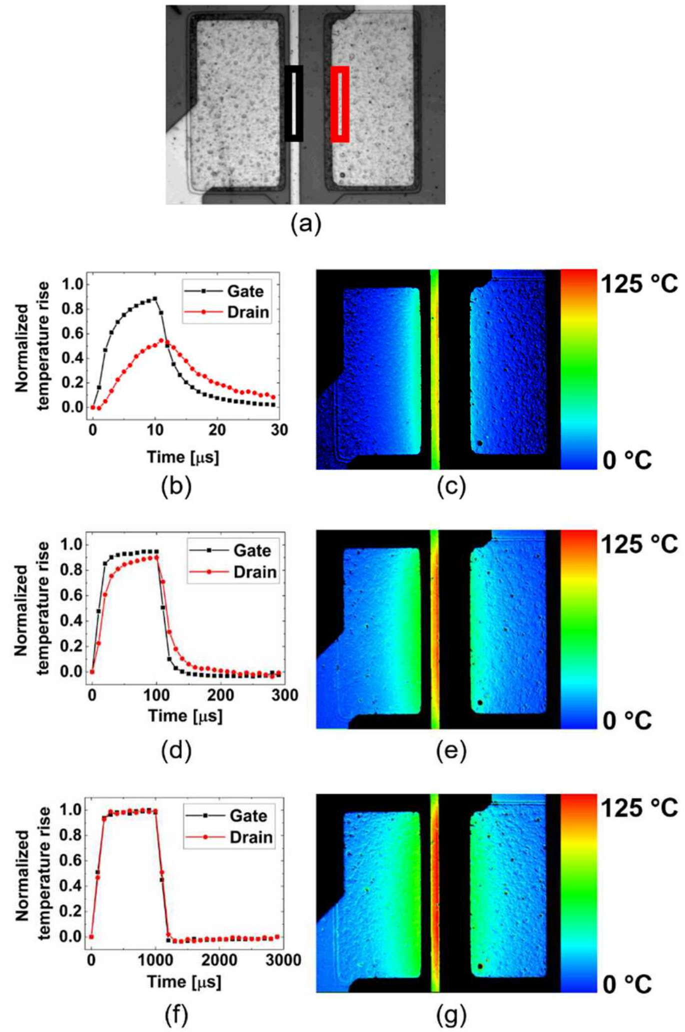

FIGURE 6: (a) Top-side view of the device highlighting the gate (black) and drain (red) regions of interest during the transient thermal characterization. (b), (d), and (f) The transient temperature rise of the gate and drain regions from (a) normalized with respect to the steady-state temperature rise of the respective region for electrical pulse widths of 10 μs, 100 μs, and 1000 μs. (c), (e), and (g) Thermal image of the device surface using visible 530 nm thermoreflectance thermal imaging for electrical pulse widths of 10 μs, 100 μs, and 1000 μs.

An extreme case demonstrating poor selection of the electrical pulse width is shown in Fig. 7. The AlGaN/GaN HEMT was biased at the same conditions as in Fig. 6 (P = 6 W/mm, V_{DS} = 28 V), however, the electrical pulse width was set to 1 μs and measured with a temporal resolution of approximately 50 ns. Under this electrical pulse width condition, the gate contact can be seen to clearly demonstrate significant temperature rise (~40 °C), yet the drain contact shows absolutely no temperature rise. If evaluating the steady-state thermal response of the device, this thermal characterization would be meaningless, but for some switching applications [52] where there are fast transient heating events, this thermal analysis can be quite useful and insightful.

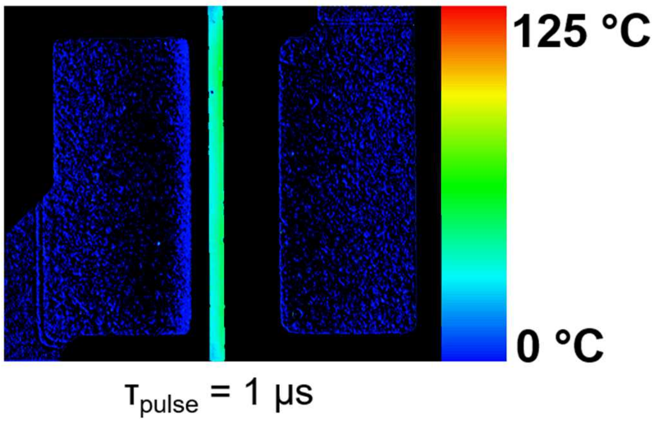

FIGURE 7: A thermal image of the device surface using thermoreflectance thermal imaging with 530 nm illumination. The thermal map was obtained for an electrical pulse width of 1 μs and an LED pulse width of 50 ns.

Using the transient measurement capabilities of both visible and ultraviolet thermoreflectance thermal imaging, the transient temperature response of the entire device surface, i.e., the lateral thermal dynamics of the device, can be determined. The Microsanj NT-210A thermoreflectance imaging system allows a temporal resolution down to 50 ns. The thermal analysis can be extended using the developed transient Raman thermometry set-up (Fig. 5) to enable integrated optical probing through the material stack thickness, i.e., the vertical thermal dynamics, of the AlGaN/GaN HEMT with a temporal resolution down to 15 ns. Using 365 nm and 530 nm LED illumination with thermoreflectance thermal imaging to respectively probe the GaN channel and metal contacts (gate, drain, and source) and nanoparticle-assisted and standard Raman thermometry to respectively probe the TiO_2 nanoparticle (surface) and Si substrate surface, the multidimensional thermal response of the device as a function of electrical pulse width can be determined and analyzed. These results are shown in Fig. 8 for the AlGaN/GaN HEMT operating with a power density of P = 6 W/mm at V_{DS} = 28 V. For measurement of the GaN channel and metal contacts with 365 nm and 530 nm LED illumination, two-dimensional point-by-point C_{TR} calibration maps were used. For 365 nm illumination of the GaN channel, the average C_{TR} was approximately -2.8×10^{-3} K^{-1}, and for 530 nm illumination of the metal contacts, the average C_{TR} was approximately -1.5×10^{-4} K^{-1}.

For the maximum electrical pulse width (1000 μs), the temperature rise in all regions of the device are seen to reach the steady-state value. The maximum temperature rises in the device are seen at the gate, drain-side of the channel, and the TiO_2 nanoparticle acting as a surface temperature transducer on the drain-side of the gate (Fig. 8). This is expected because these three locations are all nearest to the localized heat generation which occurs at the drain-side corner of the gate in the GaN channel layer. The temperature rise measured on the drain-side of the channel is observed to be slightly less than the temperature rise measured for the gate and TiO_2 nanoparticle. This discrepancy is due to edge effects occurring at the gate field plate edge [53] and finite distance between the ROI and the drain-side edge of the gate where Joule heating is concentrated [17], [19], [51]. The source-side channel temperature rise is observed to be less than on the drain-side which is understandable since the localized heat generation is on the drain-side edge of the gate. Because the drain and source Ohmic contacts are the farthest from the heat generation and the Si substrate acts as a heat sink underneath the GaN, these regions are observed to have the lowest temperature rises.

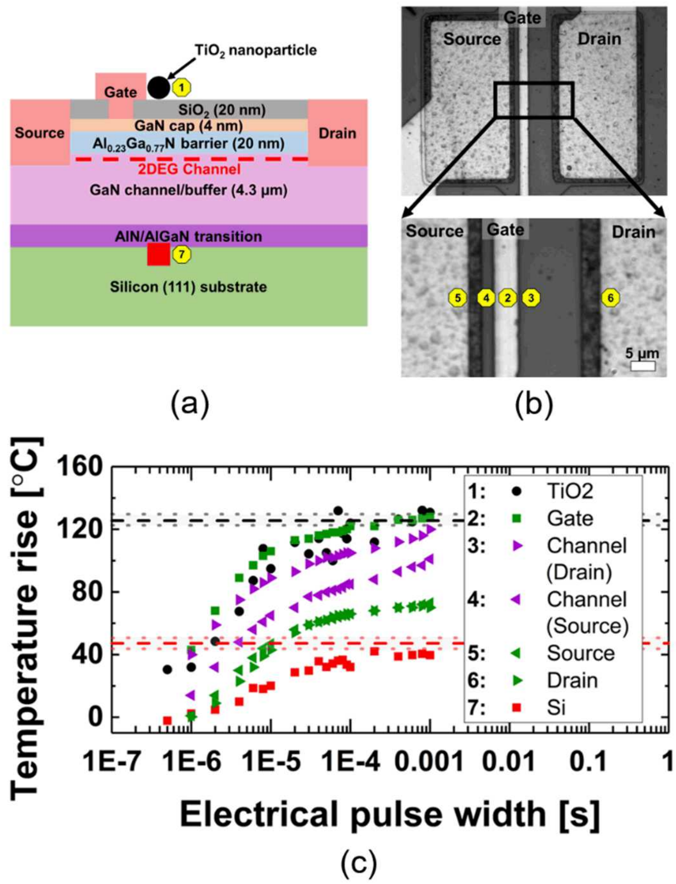

FIGURE 8: (a) Cross-sectional view of the device showing the measurement locations using nanoparticle-assisted and standard Raman thermometry; the former probes the TiO_2 nanoparticle (black sphere, 1) and the latter probes the Si substrate surface (red square, 7). (b) Top-side view of the device showing the measurements locations using ultraviolet 365 nm (3, 4) and visible 530 nm (2, 5, 6) thermoreflectance thermal imaging. (c) The temperature rise as a function of electrical pulse width for the 7 regions of interest highlighted in (a) and (b).

As the electrical pulse width biasing the device is gradually decreased, the temperature rise in all regions is seen to decrease. While the power density remains constant, reducing the electrical pulse width results in less averaged power/heat generation. As the electrical pulse width is continually decreased, a transient regime (≤ 1 μs) is reached where there is almost no measurable temperature rise in the drain and source

Ohmic contacts or the Si substrate surface. This is because the finite thermal penetration length from the heat generation source at the drain-side corner of the gate has now been reduced to a length scale less than or equal to the gate-drain and gate-source contact spacings, and the thermal penetration depth has been reduced to a length scale less than the GaN channel/buffer layer thickness. Therefore, from the integrated optical probing of the device thermal dynamics, a thermal penetration length of approximately 4-5 μm is observed at an electrical pulse width of 1 μs (10% duty cycle, 10 μs period). Due to limitations on the LED pulse width (~50 ns) using thermoreflectance thermal imaging, the minimum electrical pulse width for which the thermal response could be measured was 1 μs. However, using transient Raman thermometry with a temporal resolution of 15 ns, the electrical pulse width can be further reduced. With an electrical pulse width of 500 ns, no heating is observed in the Si substrate while a temperature rise of approximately 30 °C is measured for the TiO_2 nanoparticle at the device surface. This quantification further solidifies the concept of the finite thermal penetration depth which has been reduced to less than the thickness of the GaN channel/buffer (~4.3 μm) for a 500 ns electrical pulse width.

4. CONCLUSION

For pulsed measurement techniques such as thermoreflectance thermal imaging, it is important that the user understands the effect of the input parameters on the dynamic thermal response of the device and properly selects electrical bias inputs including the electrical pulse width and duty cycle that allow the entire device under test to reach a true steady state condition. As demonstrated in this work (Fig. 6), if the electrical pulse width is arbitrarily selected, experimental results can fail to truly capture the steady-state thermal response of the device.

However, since the electrical pulse width can be controlled as an input parameter, experiments to analyze the lateral thermal dynamics of devices can be performed. The use of both visible and ultraviolet thermoreflectance thermal imaging allows measurement of the metal contacts and semiconductor channel regions, respectively. As a result, the thermal penetration length for a given device surface geometry can be determined. In combination with standard and nanoparticle-assisted Raman thermometry, it is also possible to probe the vertical thermal dynamics of the device. From Fig. 8 it can be seen that as the pulse width is decreased, the thermal penetration depth eventually becomes less than the thickness of the GaN channel/buffer layer. This indicates that for certain power switching applications with fast transient heating events, the role of the substrate in thermal management could be insignificant.

The integrated optical probing of the thermal dynamics of the AlGaN/GaN HEMT can also be extended in order to understand the thermal dynamics of emerging ultrawide bandgap (UWBG) device technologies such as $Al_xGa_{1-x}N$ and Ga_2O_3 [54]–[59]. Since the thermal penetration length and depth are proportional to the square root of the thermal conductivity [60], the thermal response times of these UWBG device technologies are expected to increase; therefore, longer electrical pulse widths must be employed in order to measure the true steady state thermal response. To demonstrate the increased thermal response time for UWBG devices, the thermal responses of an $Al_{0.45}Ga_{0.55}N/Al_{0.30}Ga_{0.70}N$ HEMT [56] and an AlGaN/GaN HEMT from the same device die as the one used in this study with a similar device geometry (L_{gate} = 2 μm, $L_{gate\text{-}drain} = L_{gate\text{-}source}$ = 4 μm) were measured using thermoreflectance thermal imaging (530 nm illumination) with electrical pulse widths varying from 1 μs to 60 seconds (steady state) and a 10% duty cycle (Fig. 9). The steady state temperatures of each device feature (gate and drain) were used to normalize the temperature rises as a function of electrical pulse width. As shown in Fig. 9, the thermal time constants (time to reach ~63% of the steady state temperature rise) of the gate/drain contacts were ~3/~10 μs and ~30/~300 μs for the AlGaN/GaN and $Al_{0.45}Ga_{0.55}N/Al_{0.30}Ga_{0.70}N$ HEMTs, respectively. This metric quantitatively indicates the slower thermal response of the UWBG AlGaN material. The slower thermal response can also be seen qualitatively by the systematic shift in the normalized temperature rises of the $Al_{0.45}Ga_{0.55}N/Al_{0.30}Ga_{0.70}N$ HEMT as compared to the AlGaN/GaN HEMT. Therefore, for switching applications with fast transient heating events, thermal obstacles resulting from increased thermal resistances can be alleviated allowing the performance benefits from the improved electrical properties of next generation UWBG materials to be realized.

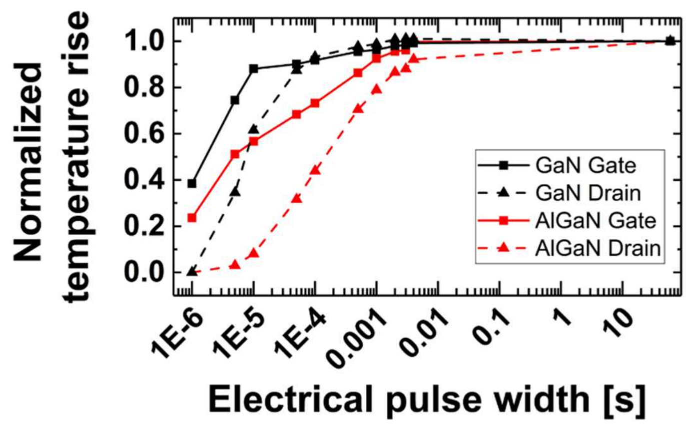

FIGURE 9: Normalized temperature rise of the gate (solid line, square symbols) and drain (dashed line, triangle symbols) contacts as a function of electrical pulse width for an AlGaN/GaN HEMT (black) and an $Al_{0.45}Ga_{0.55}N/Al_{0.30}Ga_{0.70}N$ HEMT (red) operating with a power density of P = 1.6 W/mm. The steady state (60 s) temperature rise of the gate and drain contacts of the AlGaN/GaN HEMT were 24 °C and 8 °C, respectively. The steady state temperature rise of the gate and drain contacts of the $Al_{0.45}Ga_{0.55}N/Al_{0.30}Ga_{0.70}N$ HEMT were 68 °C and 34 °C, respectively.

ACKNOWLEDGEMENTS

Funding for efforts by the Pennsylvania State University was provided by the AFOSR Young Investigator Program (Grant No. FA9550-17-1-0141, Program Officers: Dr. Michael Kendra and Dr. Brett Pokines, also monitored by Dr. Kenneth Goretta). Efforts by Hongik University were supported by the National Research Foundation of Korea (NRF) grant funded by the Korea government (MSIT) (No. 2016R1A1B4010474). Sandia National Laboratories is a multimission laboratory managed and operated by National Technology & Engineering Solutions of Sandia, LLC, a wholly owned subsidiary of Honeywell International Inc., for the U.S. Department of Energy's National Nuclear Security Administration under contract DE-NA0003525. This paper describes objective technical results and analysis. Any subjective views or opinions that might be expressed in the paper do not necessarily represent the views of the U.S. Department of Energy or the United States Government.

REFERENCES

[1] U. K. Mishra, L. Shen, T. E. Kazior, and Y. Wu, "GaN-Based RF Power Devices and Amplifiers," vol. 96, no. 2, pp. 287–305, 2008.

[2] J. J. Komiak, "GaN HEMT: Dominant Force in High-Frequency Solid-State Power Amplifiers," *IEEE Microw. Mag.*, vol. 16, no. 3, pp. 97–105, 2015.

[3] R. J. Trew, M. W. Shin, and V. Gatto, "High power applications for GaN-based devices," *Solid. State. Electron.*, vol. 41, no. 10, pp. 1561–1567, 1997.

[4] K. J. Chen *et al.*, "GaN-on-Si power technology: Devices and applications," *IEEE Trans. Electron Devices*, vol. 64, no. 3, pp. 779–795, 2017.

[5] T. Palacios *et al.*, "High-power AlGaN/GaN HEMTs for Ka-band applications," *IEEE Electron Device Lett.*, vol. 26, no. 11, pp. 781–783, 2005.

[6] J. Millan, P. Godignon, X. Perpina, A. Perez-Tomas, and J. Rebollo, "A survey of wide bandgap power semiconductor devices," *IEEE Trans. Power Electron.*, vol. 29, no. 5, pp. 2155–2163, 2014.

[7] R. S. Pengelly, S. M. Wood, J. W. Milligan, S. T. Sheppard, and W. L. Pribble, "A review of GaN on SiC high electron-mobility power transistors and MMICs," *IEEE Trans. Microw. Theory Tech.*, vol. 60, no. 6 PART 2, pp. 1764–1783, 2012.

[8] B. Ozpineci and L. M. Tolbert, *Comparison of wide-bandgap semiconductors for power electronics applications*. 2003.

[9] M. Shur and R. F. Davis, *GaN-based materials and devices: growth, fabrication, characterization and performance*, vol. 11. World Scientific, 2004.

[10] M. E. Levinshtein, S. L. Rumyantsev, and M. S. Shur, *Properties of Advanced Semiconductor Materials: GaN, AIN, InN, BN, SiC, SiGe*. John Wiley & Sons, 2001.

[11] T. J. Flack, B. N. Pushpakaran, and S. B. Bayne, "GaN Technology for Power Electronic Applications: A Review," *J. Electron. Mater.*, vol. 45, no. 6, pp. 2673–2682, 2016.

[12] O. Ambacher *et al.*, "Two-dimensional electron gases induced by spontaneous and piezoelectric polarization charges in N- and Ga-face AlGaN/GaN heterostructures," *J. Appl. Phys.*, vol. 85, no. 6, p. 3222, 1999.

[13] V. Cimalla, J. Pezoldt, and O. Ambacher, "Group III nitride and SiC based MEMS and NEMS: Materials properties, technology and applications," *J. Phys. D. Appl. Phys.*, vol. 40, no. 20, pp. 6386–6434, 2007.

[14] R. Mitova, R. Ghosh, U. Mhaskar, D. Klikic, M. X. Wang, and A. Dentella, "Investigations of 600-v gan HEMT and GaN diode for power converter applications," *IEEE Trans. Power Electron.*, vol. 29, no. 5, pp. 2441–2452, 2014.

[15] Y. Wu, M. Jacob-Mitos, M. L. Moore, and S. Heikman, "A 97.8% efficient GaN HEMT boost converter with 300-W output power at 1 MHz," *IEEE Electron Device Lett.*, vol. 29, no. 8, pp. 824–826, 2008.

[16] N. Zhang *et al.*, "Large area GaN HEMT power devices for power electronic applications: switching and temperature characteristics," pp. 233–237, 2004.

[17] S. Choi, E. R. Heller, D. Dorsey, R. Vetury, and S. Graham, "The impact of bias conditions on self-heating in AlGaN/GaN HEMTs," *IEEE Trans. Electron Devices*, vol. 60, no. 1, pp. 159–162, 2013.

[18] X. D. Wang, W. Da Hu, X. S. Chen, and W. Lu, "The study of self-heating and hot-electron effects for AlGaN/GaN double-channel HEMTs," *IEEE Trans. Electron Devices*, vol. 59, no. 5, pp. 1393–1401, 2012.

[19] E. Heller, S. Choi, D. Dorsey, R. Vetury, and S. Graham, "Electrical and structural dependence of operating temperature of AlGaN/GaN HEMTs," *Microelectron. Reliab.*, vol. 53, no. 6, pp. 872–877, 2013.

[20] J. Si, J. Wei, W. Chen, and B. Zhang, "Electric field distribution around drain-side gate edge in algan/gan hemts: Analytical approach," *IEEE Trans. Electron Devices*, vol. 60, no. 10, pp. 3223–3229, 2013.

[21] S. Sridharan, A. Venkatachalam, and P. D. Yoder, "Electrothermal analysis of AlGaN / GaN high electron mobility transistors," pp. 236–239, 2008.

[22] S. B. Lisesivdin, S. Acar, M. Kasap, S. Ozcelik, S. Gokden, and E. Ozbay, "Scattering analysis of 2DEG carrier extracted by QMSA in undoped Al 0.25Ga0.75N/GaN heterostructures," *Semicond. Sci. Technol.*, vol. 22, no. 5, pp. 543–548, 2007.

[23] S. Qu *et al.*, "Influence of the growth temperature of AlN buffer on the quality and stress of GaN films grown on 6H-SiC substrate by MOVPE," *J. Alloys Compd.*, vol. 502, no. 2, pp. 417–422, 2010.

[24] M. Ishida, T. Ueda, T. Tanaka, and D. Ueda, "GaN on Si technologies for power dwitching fevices," *IEEE Trans. Electron Devices*, vol. 60, no. 10, pp. 3053–3059, 2013.

[25] S. Choi, E. Heller, D. Dorsey, R. Vetury, and S. Graham, "The impact of mechanical stress on the degradation of AlGaN / GaN high electron mobility transistors The impact of mechanical stress on the degradation of AlGaN / GaN high electron mobility transistors," vol. 164501, no. 2013, 2015.

[26] J. A. del Alamo and J. Joh, "GaN HEMT reliability," *Microelectron. Reliab.*, vol. 49, no. 9–11, pp. 1200–1206, 2009.

[27] E. R. Heller, "Simulation of Life Testing Procedures for Estimating Long-Term Degradation and Lifetime of

AlGaN / GaN HEMTs," vol. 55, no. 10, pp. 2554–2560, 2008.
[28] J. W. Pomeroy, M. J. Uren, B. Lambert, and M. Kuball, "Operating channel temperature in GaN HEMTs: DC versus RF accelerated life testing," *Microelectron. Reliab.*, vol. 55, no. 12, pp. 2505–2510, 2015.
[29] S. Choi *et al.*, "Thermal Design and Characterization of Heterogeneously Integrated InGaP/GaAs HBTs," *IEEE Trans. Components, Packag. Manuf. Technol.*, vol. 6, no. 5, pp. 740–748, May 2016.
[30] Z. Yan, G. Liu, J. M. Khan, and A. A. Balandin, "Graphene quilts for thermal management of high-power GaN transistors," *Nat. Commun.*, vol. 3, no. May, pp. 827–828, 2012.
[31] Y. Won, J. Cho, D. Agonafer, M. Asheghi, and K. E. Goodson, "Cooling limits for GaN HEMT technology," *Tech. Dig. - IEEE Compd. Semicond. Integr. Circuit Symp. CSIC*, pp. 1–5, 2013.
[32] S. Choi, E. R. Heller, D. Dorsey, R. Vetury, and S. Graham, "Thermometry of AlGaN/GaN HEMTs using multispectral raman features," *IEEE Trans. Electron Devices*, vol. 60, no. 6, pp. 1898–1904, 2013.
[33] M. Kuball *et al.*, "Measurement of temperature in active high-power AlGaN/GaN HFETs using Raman spectroscopy," *IEEE Electron Device Lett.*, vol. 23, no. 1, pp. 7–9, 2002.
[34] K. Maize *et al.*, "High resolution thermal characterization and simulation of power AlGaN/GaN HEMTs using micro-Raman thermography and 800 picosecond transient thermoreflectance imaging," *Tech. Dig. - IEEE Compd. Semicond. Integr. Circuit Symp. CSIC*, 2014.
[35] G. Pavlidis, D. Kendig, E. R. Heller, and S. Graham, "Transient Thermal Characterization of AlGaN/GaN HEMTs Under Pulsed Biasing," *IEEE Trans. Electron Devices*, vol. 65, no. 5, pp. 1753–1758, 2018.
[36] E. Mitani, M. Aojima, and S. Sano, "A kW-class AlGaN/GaN HEMT Pallet Amplifier for S-band high power application," *Eur. Microw. Week 2007 Conf. Proceedings, EuMW 2007 - 2nd Eur. Microw. Integr. Circuits Conf. EuMIC 2007*, no. October, pp. 176–179, 2007.
[37] A. Sarua, M. Kuball, M. J. Uren, T. Martin, K. P. Hilton, and R. S. Balmer, "Integrated micro-Raman/infrared thermography probe for monitoring of self-heating in AlGaN/GaN transistor structures," *IEEE Trans. Electron Devices*, vol. 53, no. 10, pp. 2438–2447, 2006.
[38] K. Yazawa, D. Kendig, and A. Shakouri, "Thermal imaging characterization for high frequency and high power devices," *ICEP-IAAC 2015 - 2015 Int. Conf. Electron. Packag. iMAPS All Asia Conf.*, pp. 395–400, 2015.
[39] N. Killat, M. Kuball, T. M. Chou, U. Chowdhury, and J. Jimenez, "Temperature assessment of AlGaN/GaN HEMTs: A comparative study by Raman, electrical and IR thermography," *IEEE Int. Reliab. Phys. Symp. Proc.*, pp. 528–531, 2010.
[40] X. Huang, Q. Li, Z. Liu, and F. C. Lee, "Analytical loss model of high voltage GaN HEMT in cascode configuration," *IEEE Trans. Power Electron.*, vol. 29, no. 5, pp. 2208–2219, 2014.
[41] A. Nakajima, K. Takao, and H. Ohashi, "GaN power transistor modeling for high-speed converter circuit design," *IEEE Trans. Electron Devices*, vol. 60, no. 2, pp. 646–652, 2013.
[42] T. Beechem, A. Christensen, S. Graham, and D. Green, "Micro-Raman thermometry in the presence of complex stresses in GaN devices," *J. Appl. Phys.*, vol. 103, no. 12, p. 124501, 2008.
[43] G. J. Riedel *et al.*, "Nanosecond Timescale Thermal Dynamics of AlGaN/GaN Electronic Devices," *IEEE Electron Device Lett.*, vol. 29, no. 5, pp. 416–418, May 2008.
[44] M. Kuball *et al.*, "Time-Resolved Temperature Measurement of AlGaN / GaN Electronic Devices Using Micro-Raman Spectroscopy," vol. 28, no. 2, pp. 86–89, 2007.
[45] K. Maize, E. Heller, D. Dorsey, and A. Shakouri, "Thermoreflectance CCD imaging of self heating in AlGaN/GaN high electron mobility power transistors at high drain voltage," *Annu. IEEE Semicond. Therm. Meas. Manag. Symp.*, pp. 173–181, 2012.
[46] D. Kendig, A. Tay, and A. Shakouri, "Thermal Analysis of Advanced Microelectronic Devices Using Thermoreflectance Thermography," 2016, pp. 21–23.
[47] Y. S. Ju and K. E. Goodson, "Short-Time-Scale Thermal Mapping of Microdevices Using a Scanning Thermoreflectance Technique," *J. Heat Transfer*, vol. 120, no. 2, p. 306, 2008.
[48] D. A. Long, "Raman spectroscopy," *New York*, pp. 1–12, 1977.
[49] N. J. Everall, "Confocal Raman Microscopy: Performance, Pitfalls, and Best Practice," *Appl. Spectrosc.*, vol. 63, no. 9, pp. 245A-262A, 2009.
[50] J. Dallas *et al.*, "Thermal characterization of gallium nitride p-i-n diodes," *Appl. Phys. Lett.*, vol. 112, no. 7, 2018.
[51] E. R. Heller and A. Crespo, "Electro-thermal modeling of multifinger AlGaN/GaN HEMT device operation including thermal substrate effects," *Microelectron. Reliab.*, vol. 48, no. 1, pp. 45–50, 2008.
[52] I. Omura, W. Saito, T. Domon, and K. Tsuda, "Gallium nitride power HEMT for high switching frequency power electronics," in *2007 International Workshop on Physics of Semiconductor Devices*, 2007.
[53] G. Pavlidis, D. Kendig, L. Yates, and S. Graham, "Improving the Transient Thermal Characterization of GaN HEMTs," *Proc. 17th Intersoc. Conf. Therm. Thermomechanical Phenom. Electron. Syst. ITherm 2018*, pp. 208–213, 2018.
[54] A. G. Baca *et al.*, "An AlN/Al0.85Ga0.15N high electron mobility transistor," vol. 033509, no. 2016, pp.

0–4, 2017.
[55] A. G. Baca *et al.*, " Al 0.85 Ga 0.15 N/Al 0.70 Ga 0.30 N High Electron Mobility Transistors with Schottky Gates and Large On/Off Current Ratio over Temperature ," *ECS J. Solid State Sci. Technol.*, vol. 6, no. 12, pp. Q161–Q165, 2017.
[56] A. G. Baca *et al.*, " High Temperature Operation of Al 0.45 Ga 0.55 N/Al 0.30 Ga 0.70 N High Electron Mobility Transistors ," *ECS J. Solid State Sci. Technol.*, vol. 6, no. 11, pp. S3010–S3013, 2017.
[57] K. D. Chabak *et al.*, "Sub-Micron Gallium Oxide Radio Frequency Field-Effect Transistors," *2018 IEEE MTT-S Int. Microw. Work. Ser. Adv. Mater. Process. RF THz Appl. IMWS-AMP 2018*, pp. 1–3, 2018.
[58] A. J. Green *et al.*, "β-Ga_2O_3 MOSFETs for radio frequency operation," *IEEE Electron Device Lett.*, vol. 38, no. 6, pp. 790–793, 2017.
[59] M. H. Wong, K. Sasaki, A. Kuramata, S. Yamakoshi, and M. Higashiwaki, "Field-plated Ga_2O_3 MOSFETs with a breakdown voltage of over 750V," *IEEE Electron Device Lett.*, vol. 37, no. 2, pp. 212–215, 2016.
[60] Y. K. Koh and D. G. Cahill, "Frequency dependence of the thermal conductivity of semiconductor alloys," *Phys. Rev. B - Condens. Matter Mater. Phys.*, vol. 76, no. 7, pp. 1–5, 2007.